Available online at www.sciencedirect.com
ScienceDirect
Colloids and Surfaces B: Biointerfaces 58 (2007) 52–60
COLLOIDS AND SURFACES B
www.elsevier.com/locate/colsurfb

A low-cost, disposable card for rapid polymerase chain reaction

Guangyao Jia [a], Jonathan Siegrist [a], Chengwu Deng [a], Jim V. Zoval [a], Gale Stewart [b], Regis Peytavi [b], Ann Huletsky [b], Michel G. Bergeron [b], Marc J. Madou [a,*]

[a] *Department of Mechanical & Aerospace Engineering, University of California at Irvine, Irvine, CA 92697, United States*
[b] *Centre de Recherche en Infectiologie de l'Université Laval, Centre Hospitalier, Universitaire de Québec (Pavillon CHUL), Sainte-Foy, Québec, Canada*

Available online 13 March 2007

Abstract

A low-cost, disposable card for rapid polymerase chain reaction (PCR) was developed in this work. Commercially available, adhesive-coated aluminum foils and polypropylene films were laminated with structured polycarbonate films to form microreactors in a card format. Ice valves [1] were employed to seal the reaction chambers during thermal cycling and a Peltier-based thermal cycler was configured for rapid thermal cycling and ice valve actuation. Numerical modeling was conducted to optimize the design of the PCR reactor and investigate the thermal gradient in the reaction chamber in the direction of sample thickness. The PCR reactor was experimentally characterized by using thin foil thermocouples and validated by a successful amplification of 10 copy of *E. coli tuf* gene in 27 min.

Keywords: PCR amplification; Disposable card; Ice valve; Miniaturization; Modeling

1. Introduction

Since its advent, polymerase chain reaction (PCR) [2] has become an indispensable tool for *in vitro* amplification of DNA in molecular biology, forensic analysis, and medical diagnostics. PCR requires thermal cycling of the sample, and the speed of temperature transitions and the thermal homogeneity throughout the PCR mixture are essential for the run time, efficiency and specificity of the amplification reactions [3]. To attain rapid temperature transitions while maintaining high thermal homogeneity in the PCR mixture, a low thermal mass of the entire system and efficient heat transfer through the thermal path are prerequisites. For most conventional PCR systems, heating and cooling rates are relatively slow due to the large thermal masses of the thermal cyclers and inefficient heat transfer resulting from the low surface-to-volume ratio (SVR) of sample containers and unfavorable thermal properties of container materials (e.g. polypropylene and polyester). Consequently, run times are typically in excess of 90 min [4]. It is the art of miniaturization that has provided an effective approach to reduce the thermal inertia and increase the SVR so as to attain rapid temperature cycling. With this idea in mind, various miniaturized PCR devices have been developed.

Most of the early miniaturized PCR devices were fabricated in silicon or glass by taking advantage of well-established microfabrication technologies [5–12]. However, polymeric materials have been explored as more versatile alternatives for fabrication of microfluidic PCR devices [13–20]. Unfortunately, low thermal diffusivities of commonly used polymers have limited the further improvement on speed of thermal response in polymeric PCR reactors. In this work, we report a planar miniaturized PCR device that merges the favorable properties of both metallic and polymeric materials by combining a commercially available aluminum (Al) foil with plastic as construction materials. Experiment and numerical simulation of transient heat transfer were conducted to systematically investigate the effects of sample thickness and material properties on the performance of the reactor. Experimental verification on the thermal gradient in the direction of sample thickness was performed using thin foil thermocouples laminated into the chamber. We also present an improved ice valve approach [21] for sealing the reaction chamber during thermal cycling and a custom-configured Peltier thermal cycler for rapid temperature cycling and ice valve actuation. The entire PCR system was validated by a rapid amplification of a portion of an *E. coli tuf* gene.

* Corresponding author. Tel.: +1 949 824 6585; fax: +1 949 824 8585.
E-mail address: mmadou@uci.edu (M.J. Madou).

0927-7765/$ – see front matter © 2007 Elsevier B.V. All rights reserved.
doi:10.1016/j.colsurfb.2007.03.007

2. Materials and methods

2.1. Modeling

As the first step, a 1D model was developed to theoretically investigate the relationship between the depth of the reaction chamber and the thermal response given a specified heater temperature profile. Based on the simulation results, design depth and other dimensions of the reactor were determined by taking into consideration the sample volume and valid heating area of the thermal cycler described in the following section. A 3D transient model was subsequently established utilizing the design parameters of the microreactor to predict its performance and understand the effects of materials choice for the heated (bottom) side.

2.2. Design and fabrication of the disposable PCR card and top plate

A PCR reactor was designed based on the results from 1D simulation. The reactor consists of a reaction chamber (volume: 25 μL), inlet/outlet/ice valves (1 mm circles) on each side and connecting channels (0.3 mm wide). As shown in Fig. 1A, four reactors are arranged in a planar format on a footprint area of 78 mm × 36 mm. The PCR card contains three layers, as illustrated in Fig. 1B: a structured polycarbonate (PC) film in the middle, a polypropylene (PP) film and an aluminum (Al) foil on the top and bottom side of the PC film, respectively. Four 3.18 mm (diameter) alignment holes were designed on the corners of the card to facilitate assembling the PC part with the film on the top. The open structures of the chambers, channels, ice valves and four alignment holes in the middle layer (0.25 mm thick PC film (G.E. Plastics)) were created using a computer-controlled vinyl cutter (Western Graphtec, Irvine, CA), and the top film was obtained by patterning a ThermalSeal film (Excel Scientific, Wrightwood, CA) using the same cutter. The top and middle films were aligned and laminated using a custom-made assembling jig, followed by sealing an AlumaSeal II foil (Excel Scientific, Wrightwood, CA) on the open side. The three layers were bonded together by taking advantage of the adhesives on the ThermalSeal films and AlumaSeal II foils. Since both the ThermalSeal film and AlumaSeal II foil are commercial products for sealing PCR microplates, PCR inhibition from these materials is not an issue. To evaluate the vertical direction thermal gradient in the chamber, two T-type thin foil thermocouples (RdF Corporation, Hudson, NH) were attached to the inner (adhesive) side of the top film and bottom foil (see Fig. 1A and B) at the center of the chamber. This card was also used for calibrating the control system. For the cards used in the amplification experiment, *in situ* temperature measuring was not necessary.

In order to improve thermal contact between the PCR card and the heating/cooling surface on the thermal cycler described below, a top plate (see Fig. 1C) was designed to clamp down two PCR cards (for parallel runs) firmly against the heaters. The top

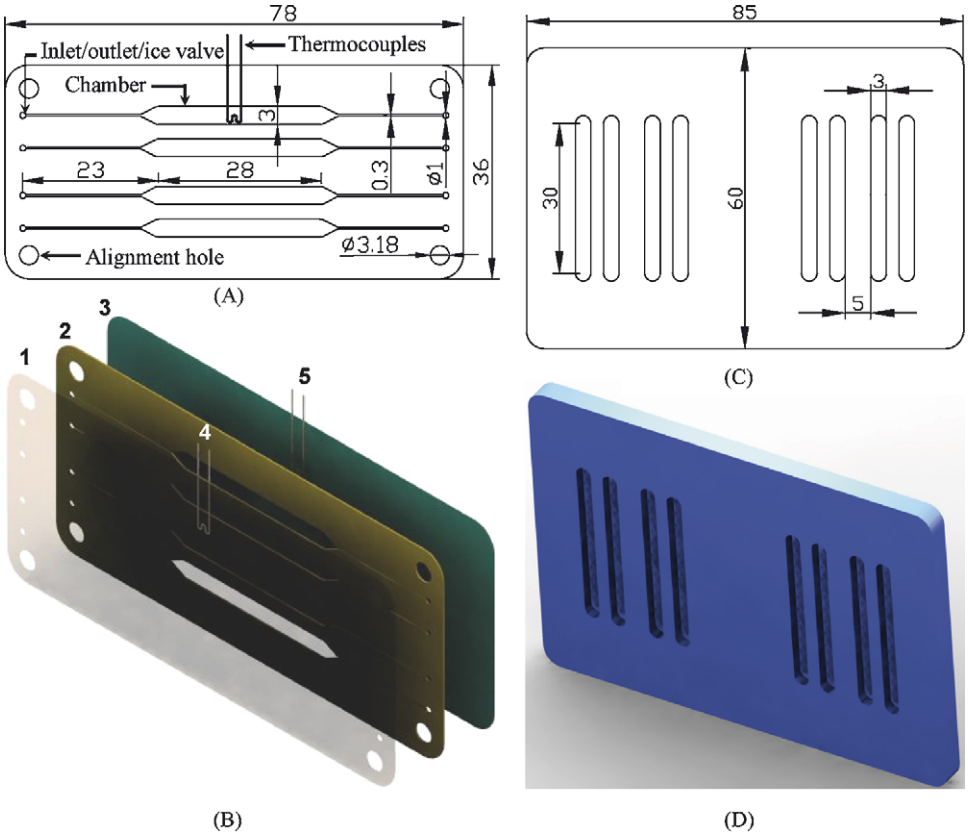

Fig. 1. Design of PCR card and top plate. (A) Layout of PCR card with thermocouples. (B) Rendering of PCR card assembly: (1) PP film; (2) structured PC sheet; (3) Al foil; (4) thermocouple, top; (5) thermocouple, bottom. (C) Layout of top plate. (D) Rendering of top plate.

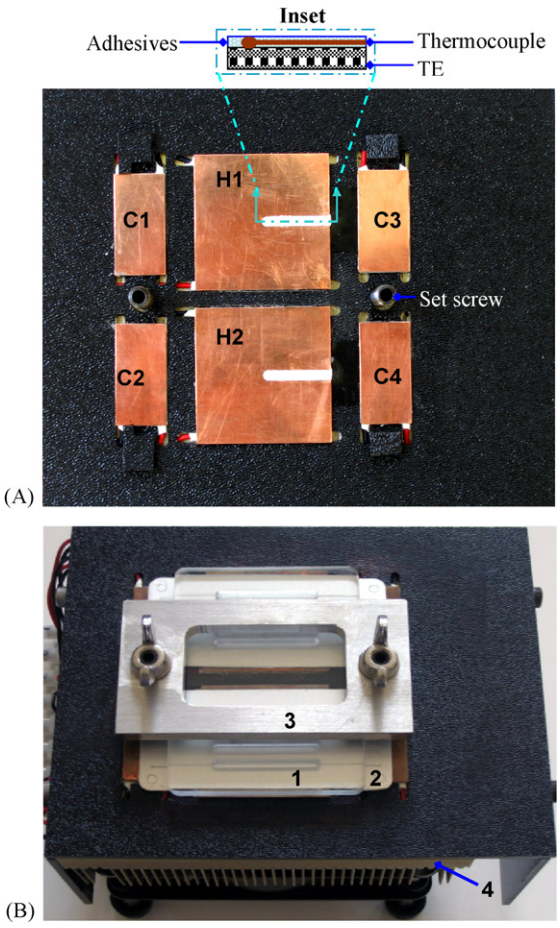

Fig. 2. Thermal cycler. (A) Top view, TE modules in ABS template. C1–4 are TE modules for ice valves; H1, 2 are TE modules for heating. Inset: schematic of cross-section of the thermocouple embedded in aluminum adhesives. (B) PCR card on thermal cycler: (1) top plate; (2) PCR card; (3) metal frame set; (4) heat sink assembly (heat sink + axial flow fan).

plate was machined from a 4.75 mm acrylic sheet using a CNC machine (T-Tech, Atlanta, GA), as illustrated in Fig. 1D. To minimize resultant thermal load to the reactor, grooves (2 mm deep) were milled corresponding to the chambers in the cards so that air pockets could be formed on the top of the PCR chambers. Since the thermal conductivity and density of air are significantly lower than those of the plastic, less thermal capacitance is expected and consequently, faster heating and cooling speed can be achieved compared to a solid top plate of the same thickness.

2.3. Configuration of the thermal electric-based thermal cycler

A Peltier-based thermal cycler was configured in our lab. As shown in Fig. 2, the thermal cycler consists of six thermal electric (TE) modules (Ferrotec, New Hampshire, NJ) and a heat sink (C&H Technology, MN) equipped with an axial fan (Newark, NJ) for forced convection. The two TE modules (effective heating area for each: 40 mm × 40 mm) in the middle of the heat sink were used for thermal cycling while the four (15 mm × 30 mm) on two sides were used for ice valve actuation. All the TE modules were held in position using a CNC-machined acrylonitrile butadiene styrene (ABS) template. Interfacial material (Arctic Silver 5, Visalia, CA) was applied at the interface between the TEs and the heat sink to reduce thermal contact resistance.

To attain spatial thermal homogeneity across the heating surfaces, 0.44 mm thick pure copper sheets were attached on the top of the TEs using Arctic Silver 5. A 2 mm × 20 mm slot was cut in the middle of each copper sheet to accommodate a thermocouple (Omega, Stamford, CT) that was glued to the TE surface using Arctic Alumina adhesives (Visalia, CA), as shown in Fig. 2A. These thermocouples are used to acquire the temperatures of the TE surfaces for profile control. Fig. 2B shows a picture of the assembly. Two cards were positioned on the thermal cycler for a parallel run using an aluminum frame and two set-screws, including washers and wing nuts.

2.4. Power supply and control system

The TE modules were powered by an Agilent power supply N6711A (Agilent Technologies, Palo Alto, CA) that contains four power modules in an N6701A mainframe. The power modules have polarity-switching options for heating and cooling using the same TEs. The power supply was interfaced with National Instruments (NI) LabVIEW software via a USB port. The thermocouples on the TE surfaces were connected to a NI SC-2345 signal-conditioning box to filter noise common with thermocouple readings. The signal-conditioning box was interfaced with a PC using a NI 6221 DAQ System.

Temperature control for thermal cycling was implemented using the PID (proportional–integral–derivative) Control Toolset in LabVIEW. A gain scheduling scheme, consisting of three sets of PID parameters for temperature maintaining and three sets of PD parameters for temperature transitions, was utilized to attain rapid thermal cycling with optimal temperature control.

2.5. Experimental characterization of PCR reactor

Before the amplification validation shown below, the control system was calibrated using the card equipped with thin foil thermocouples so that the temperature on the TE surface was properly correlated with temperature in the reaction chamber. The PCR card with thermocouples was also used to investigate the thermal gradient in the direction of depth of the reaction chamber during thermal cycling. A temperature profile of 3 s, 7 s and 10 s for denaturation at 95 °C, annealing at 60 °C and extension at 72 °C, respectively, was used for an *in situ* study of the thermal response of the micro-PCR reactor.

2.6. Amplification of E. coli tuf gene

DNA amplification using the PCR system we developed was validated by amplification of a 210 bp region of *E. coli tuf* gene. Three concentrations of purified DNA ranging from 10 to 1000 *E. coli* ATCC 35401 genome copies were used in the experiments to explore the lower limit of detection of the PCR device. Forward and reverse primers were Teco553 (TGGGAAGCGAAAATCCTG) and Teco754

(CAGTACAGGTAGACTTCTG). Taq polymerase (Promega, Madison, WI) at 0.025 U/reaction and TaqStart™ antibody at 1.1 ng/reaction (Clontech, Mountain View, CA) were used in the Promega 10X PCR buffer.

The PCR mixture was loaded into the card using a pipette (Eppendorf). A mixture without DNA template was used as a negative control. The card was positioned on the thermal cycler using the top plate and the metal frame set. The TE modules for the ice valves were switched on to actuate the ice valves 1 min before starting thermal cycling. Hot start was achieved through denaturation of the TaqStart™ antibody at 95 °C for 1 min. A 40-cycle amplification was conducted using a temperature profile of 7 s 15 s and 15 s (ramping times included) for denaturation at 95 °C, annealing at 60 °C and extension at 72 °C, respectively. Upon completion of amplification, the card was dismounted from the thermal cycler. The samples were unloaded from the chambers and 1.0 μL of sample was injected into an Agilent BioAnalyser 2100 cartridge (Agilent Technologies, Palo Alto, CA) for detection.

3. Results and discussion

3.1. Thermal cycler

Thermal electrics have been used widely in microfluidic PCR devices [19,22,23]. An important reason for the broad applications of TEs in thermal cyclers lies in that active cooling can be realized in the same module simply by switching the polarity of the applied voltage. Therefore, higher cooling rates can be attained in a TE-based thermal cycler compared to passive cooling cyclers. In addition, the characteristics of the thermal electric are well suited for the applications in which precise temperature control is critical [24]. In this work, we configured a Peltier thermal cycler that was used for both temperature cycling and ice valve actuation.

Since the input signals to the PID control loop were obtained from the thermocouples on the TE surfaces, *in situ* temperature acquisition was not necessary once the control system was calibrated using a custom fluidic card with thermocouples inside the chamber. This has greatly simplified the fabrication process and operation procedure and reduced the cost of the disposable card as well.

3.2. Ice valves

In a PCR microreactor, bubble formation during thermal cycling is unavoidable. The bubbles may expel the PCR mixture from the PCR chamber if it is not sealed. By sealing the PCR chamber during thermal cycling, bubble formation can be minimized because of pressurization of the chamber [21]. The ice valve was used in the PCR card for this purpose as it is non-invasive, has no moving parts, and is simple to construct and operate. In addition, it does not introduce any foreign materials into the system. In the PCR card we developed, the inlets/outlets of the reactors were utilized as the ice valves during thermal cycling based on our observation that the liquid at the inlets/outlets was frozen faster than that in the channel (data not shown). Therefore, no additional fluidic structures were needed specifically for the valves. The dead volume of the reactor, which adversely affects the amplification efficiency, was 2 μL (8% of the sample volume).

3.3. Modeling

The 1D model was built to provide a guideline for the design of the reactor, while the 3D model was developed to predict the thermal response of it and explore the effects of materials for the heated side. The 3D model was also utilized to investigate the effect of the air pocket for insulation.

3.3.1. 1D modeling

Single side-heated water slabs of various thicknesses are used as 1D models to explore the effect of sample thicknesses on performance of the PCR microreactor. The model is defined mathematically as

$$\frac{\partial^2 T}{\partial z^2} = \frac{1}{\alpha}\frac{\partial T}{\partial t} \tag{1}$$

$$T(z, 0) = T_0 \tag{2}$$

$$T|_{z=0} = T_s \tag{3}$$

$$\left.\frac{\partial T}{\partial z}\right|_{z=h} = 0 \tag{4}$$

where T is the temperature (K), z the coordinate in the vertical (depth) direction (m), t the time (s), α the thermal diffusivity (m^2/s), T_0 the initial temperature (K), T_s the prescribed surface temperature (K), and h is the thickness of the slab (m). At $z = h$, the analytical solution to the above equation is adapted from Bird et al. [25]:

$$\theta = \frac{T - T_s}{T_0 - T_s} = 2\sum_{n=0}^{\infty} C_n \, e^{-(n+(1/2))^2 \pi^2 (\alpha/h^2) t} \tag{5}$$

where θ is a dimensionless criterion that can be used to evaluate the temperature relatively. The coefficient C_n is

$$C_n = \frac{(-1)^n}{(n + (1/2))\pi} (n = 0, 1, 2, 3 \ldots \infty) \tag{6}$$

Eq. (5) reveals that a small magnitude of variation in the slab thickness results in a significant change in θ as it is approximately proportional to the exponential of h^2. To quantitatively explore the response of the models to temperatures varying with time, CFDRC software (Huntsville, AL) is used and a single temperature cycle is applied on the bottom of the slab to mimic a thermal cycling process starting from denaturation temperature (95 °C). Adiabatic boundary conditions are applied on the top of the model. The heating and cooling rates (i.e. the slopes of the profile during transitions) are chosen to be 10 °C/s, which is approximately the heating and cooling rate of the thermal cycler we built. The total time (ramping time + holding time) at each temperature is 15 s. Three model thicknesses, 1 mm, 0.5 mm and 0.25 mm are investigated individually.

Table 1
Rayleigh numbers in heating processes

	Model 1 (1 mm)	Model 2 (0.5 mm)	Model 3 (0.25 mm)
$Ra_{72\,^\circ C \to 95\,^\circ C}$	2700	338	42
$Ra_{60\,^\circ C \to 72\,^\circ C}$	985	123	15

To verify if natural convection plays a role in the heating processes, the Rayleigh number is evaluated using the following equation [26]:

$$Ra = \frac{g\beta(T_1 - T_2)h^3}{\alpha\nu} \tag{7}$$

where Ra is the Rayleigh number for a 2D cavity, g gravitational acceleration (m/s^2), β the volumetric thermal expansion coefficient (K^{-1}), α the thermal diffusivity, as previously described, ν the kinematic viscosity (m^2/s), T_1 and T_2 bottom and top temperatures, respectively (K), and h is the depth of the cavity (m).

For Rayleigh numbers less than a critical value of Ra,$c = 1708$, buoyancy forces cannot overcome the resistance imposed by viscous forces and there is no advection in the cavity. Hence heat transfer from the bottom to the top surface is dominated by conduction [26]. By inserting the temperatures, the liquid thickness and the related physical properties evaluated at average temperature for the heating processes, the Rayleigh numbers are obtained and listed in Table 1.

Since the Rayleigh number for Model 1 is 2700, greater than Ra, $c = 1708$, natural convection is taken into account in this model. The Rayleigh numbers for Models 2 and 3 are well below the critical number and consequently heat transfer by conduction is exclusively considered in these models.

Predicted temperatures at the top of the liquid are compared in Fig. 3, and boundary temperatures of the heated side are plotted as a reference. It is obvious that upon the same prescribed temperature profile, differences in thermal response speed at the top of the liquid are significant in the three models. Model 1 responds sluggishly, while Model 3 responds rapidly to the boundary temperatures. The response of Model 2 is slightly slower than Model 3 but significantly faster than Model 1. In terms of average response speed, which is defined as $(T_d - T_a)/\Delta t$ (T_d and T_a represent denaturation and annealing temperature, respectively; Δt is the time for the transition from T_d to T_a), Model 3 is 42% faster than Model 2 and 277% faster than Model 1.

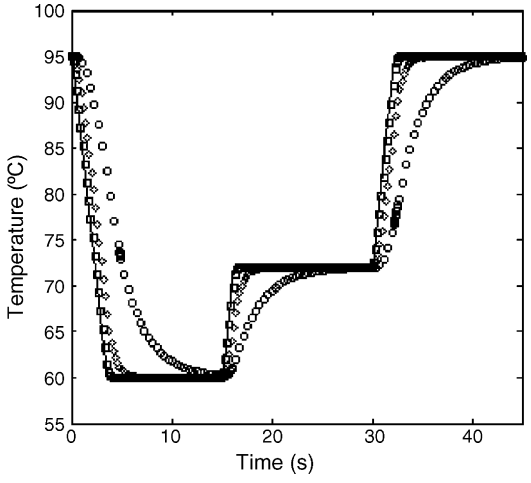

Fig. 3. Comparison of thermal responses of the 1D models. Open circle: Model 1; open diamond: Model 2; open square: Model 3; solid line: boundary.

The 1D modeling results show that the temperature transition speed in a reaction chamber is highly responsive to the depth of the reactor, consistent with the analysis using Eq. (5). It should be noted that the response profile of Model 3 resembles the reference temperature profile, suggesting a decent match between the thermal response speed of the model and the prescribed heating/cooling rate (10 °C/s). In brief, the temperature transition speed in a reaction chamber is determined not only by the heating/cooling rate of the thermal cycler, but the thermal response speed of the PCR reactor. Hence, the heating/cooling rate of the thermal cycler should be considered as a foundation for the design of a reactor. Under-match (i.e. thermal response speed of the reactor to an instant transition $\ll$ heating/cooling rate of the thermal cycler) between these two parameters results in inefficient use of heating/cooling capacity on the cycler, while over-match (opposite to under-match) results in inefficient use of valid heating area.

Although convection is considered in Model 1, the thermal response speed of it is still the lowest. The reason could be that the velocity of the internal flow is not sufficiently fast to dominate heat transfer in the vertical direction, and this is evidenced by the small Peclet number ($\sim$0.17) evaluated using the simulation results.In order to evaluate the general performance of a reactor upon a specific temperature profile, mean thermal gradient $\bar{T}_{grad}$ is defined:

$$\bar{T}_{grad} = \frac{\int_{t_1}^{t_2} (T_b(t) - T_t(t))\ dt}{t_2 - t_1} \tag{8}$$

where T_b and T_t are the bottom and top temperature, and t_1 and t_2 are starting and ending times of desired temperatures at the boundary, respectively. The values of the mean temperature gradient of the three models are calculated and summarized in Table 2 based on the 1D modeling results.

Table 2
Mean temperature gradient

	$\bar{T}_{grad}$ (°C)
Model 1	
60 °C	−4.35
72 °C	1.76
95 °C	3.04
Model 2	
60 °C	−0.33
72 °C	0.23
95 °C	0.28
Model 3	
60 °C	−0.02
72 °C	0.01
95 °C	0.01

The mean temperature gradient can be used as a criterion to estimate temporally the thermal homogeneity (which is critical for amplification efficiencies) in the PCR mixture at dwell temperatures. In ideal cases, $\bar{T}_{grad}$ and $\Delta\bar{T}$ are zero as the temperature in the liquid follows the desired profile without deviation. By combining the mean thermal gradient criterion with the thermal response speed standard, a quantitative method is established for performance evaluation of a PCR reactor.

From the data in Table 2, significant differences in $\bar{T}_{grad}$ can be observed in the three models. Although the thickness of the three models doubles starting from 0.25 mm, the mean thermal gradient varies by a factor of over 15. The model with smallest thickness gives the lowest $\bar{T}_{grad}$. In the same model, however, the magnitude of variations for different transitions is small. Based on the results from the 1D modeling, we chose 0.25 mm for the depth of the PCR reactor.

3.3.2. 3D modeling

The 1D simulation results reveal the significance of sample thickness. In a real PCR reactor, wall thickness of the reaction chamber, specifically the thickness of the material for the heated side in a planar microreactor, also plays an important role for thermal response speed. Small thickness of the heated side is favorable for fast thermal response in a PCR reactor and this constitutes the reason for using thin films for chamber capping [27]. However, the gain by reducing the thickness of the heated side is limited by the availability of the materials of smallest thickness and the compatibility with bonding processes. The analytical solution to the heat equation also proves the inverse exponential dependence of thermal response on the thermal diffusivity of the materials, suggesting an additional approach in principle to push the limit of thermal response speed further. By choosing the Al foil as a capping material that is compatible with the fabrication process and PCR protocol, significant improvement on thermal response speed is expected in comparison to the PP film.

In the 3D model, the top plate is also considered to understand the effect of the air pockets. Thus, the entire model consists of bottom layer, liquid, top layer, insulating air pocket and top plate. The bottom side of the model is subject to the same temperature profile as applied in the 1D model, except that an initial denaturation step at 95 °C for 60 s is added, and the top surface of the top plate is exposed to natural convection of air in the lab environment. Two different materials, Al foils and PP films of the same thickness (0.04 mm PP base + 0.02 mm acrylic adhesives), are considered in the model to investigate theoretically the effect of materials on performance of the reactor.

Figs. 4 and 5 show the 3D modeling results for two reactors with aluminum foil and polypropylene film as heated side, respectively. The geometric model (a quarter of a reaction chamber is taken into account to minimize computational load) is illustrated in Fig. 4A. Temperature contours of the 3D model for the reactor with aluminum foil at 65 s is adopted to demonstrate the effects of the air pocket above the reactor. As shown in Fig. 4B, the thermal gradient in the chamber is negligible compared to other portions of the model. The effect of the air pocket can be further verified by comparing the thermal responses of

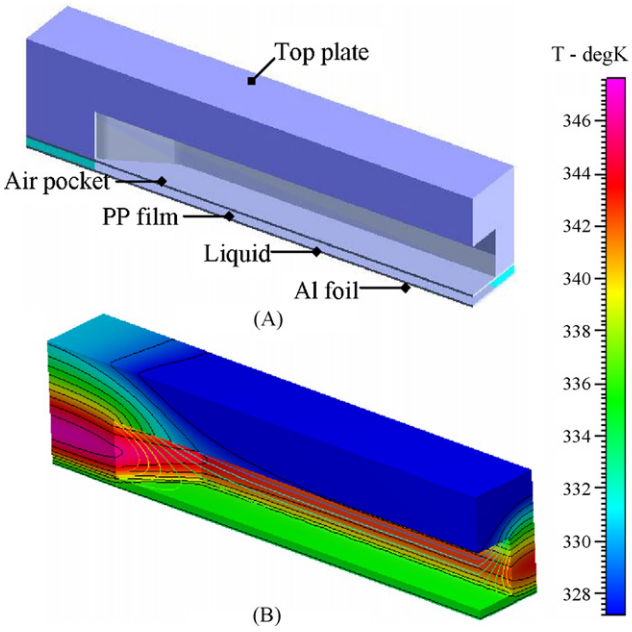

Fig. 4. Temperature contours of the 3D model. (A) Geometric model of a quarter of the reactor with grooved top plate. (B) Temperature contours for the reactor with Al foil at 65 s.

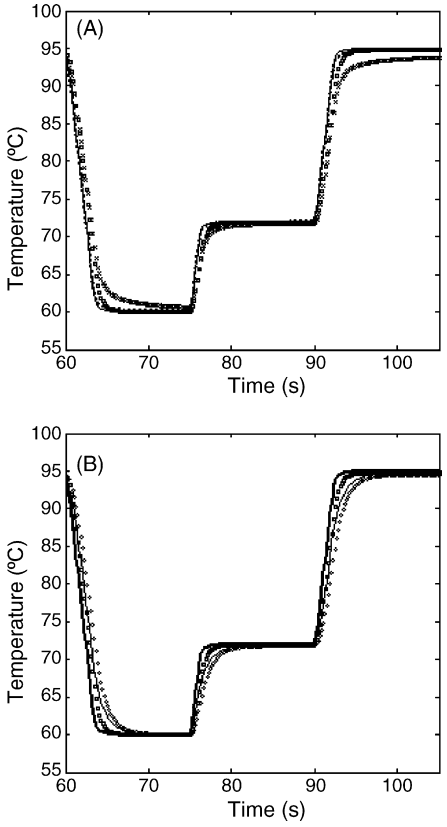

Fig. 5. Thermal responses of 3D the model. (A) Comparison of temperature profiles in a reactor with Al foil, GTP vs. STP. Solid line: bottom, GTP; dotted line: bottom, STP; open square: top, GTP; cross: top, STP. (B) Comparison of temperature profiles, Al vs. PP. Thick solid: Al-bottom; open square: Al-top; thin solid: PP-bottom; open diamond: PP-top.

the reactor clamped with the grooved top plate (GTP) to the same reactor with a solid top plate (STP). The thermal response speed in the reactor with solid top plate is significantly lower than that in the reactor with air pocket (see Fig. 5A). This is attributed to the low thermal mass and conductivity of air. The low density and heat capacity of air reduce the extra thermal load to a negligible level, while its low thermal coefficient allow excellent insulation to the reactor preventing heat loss from the top plate. In brief, the application of the air pocket has afforded a fast thermal response in the reactor.

The temperature profiles for the bottom and top side of the liquid at the center of the reactors are compared in Fig. 5B. A one-fold difference can be seen in the average thermal response speed between the two reactors. This demonstrates the significant improvement that can be achieved using material of high thermal diffusivity (the thermal diffusivity of Al is two order higher than that of PP) as the heated side of the PCR reactor. In addition, the difference in the thermal response speed between the bottom and top of the reactor with Al foil is comparable to the results from 1D modeling.

3.4. Experimental characterization of PCR reactor

Previous theoretical analysis has demonstrated the significant advantage of an Al foil over a PP film. Therefore, the Al foil was selected as the capping material for the heated side of the PCR reactor. For the top side of the reactor, PP film was used for convenience in loading and sampling afforded by its optical transparency.

Although various miniaturized PCR devices have been developed, to our knowledge, none of the devices has been experimentally investigated on the temperature gradient in reactors due to the difficulty in measuring the temperature difference *in vitro* (in the direction of the sample thickness) without perturbing the thermal system. For instance, a thin thermocouple (diameter 0.2 mm) was used to measure the sample temperature in a glass capillary (inner diameter 0.5 mm) for rapid DNA amplification [28]. Obviously the thermal gradient in the radial direction could not be measured using this set up. In addition, the disturbance caused by differences in thermal diffusivities between the sample and the materials for the thermocouple is unavoidable considering the relative dimensions of the capillary and the thermocouple. In our work, we used thin foil thermocouples that could be attached to the top and bottom surfaces inside chamber so that temperature differences in the depth direction could be measured independently. Since the thickness of the thermocouple (12.5 μm) is significantly smaller than the depth of the chamber (250 μm), the disturbance introduced by it is negligible.

Fig. 6A shows the thermal response of the PCR reactor to a five-cycle temperature profile following a 60 s initial denaturation step. The temperatures were acquired using the thin foil thermocouples attached to the bottom and top surfaces inside the reaction chamber. The heating and cooling rate was around 10 °C/s. Fig. 6B is a magnification of a single temperature cycle. It should be noted from the plot that differences in average thermal response speed between the bottom and top of the reactor

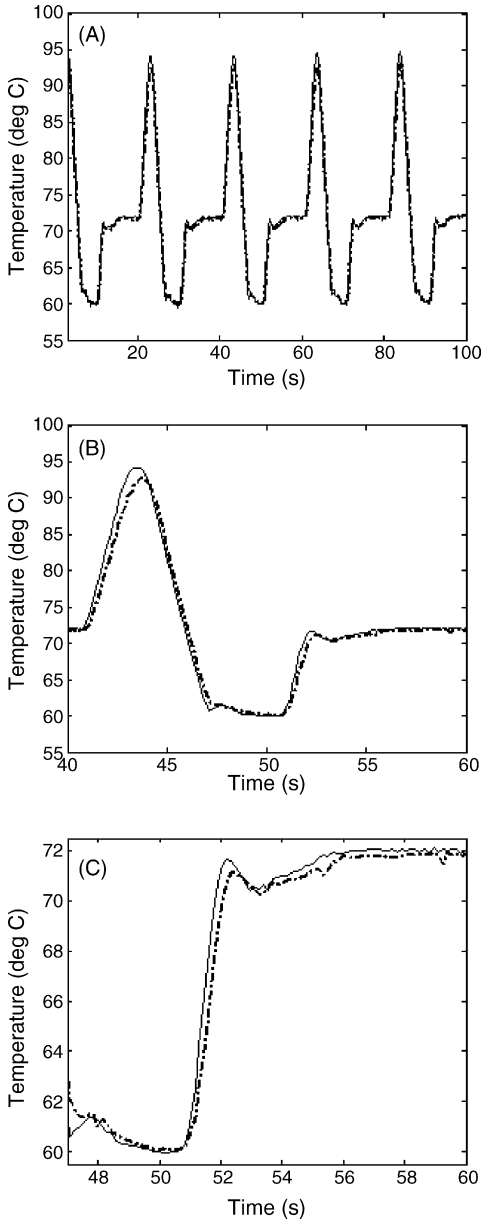

Fig. 6. Experimental characterization of a reactor with Al foil. Solid: temperature at the bottom side; dash-dotted: temperature at the top side. (A) Temperature profile—denaturation: 3 s at 95 °C; annealing: 7 s at 60 °C; extension: 10 s at °C; transition times included. (B) Magnification of single cycle profile. (C) Temperature difference at 60 °C and 72 °C.

were particularly small. This is consistent with the prediction in 1D and 3D modeling. The temperature gradient at 95 °C was relatively high, around 2 °C. An explanation on the relatively large difference at denaturation temperature is that thermal equilibrium had not been reached due to the short amount of denaturation time. Since the optimal temperature for denaturation is 91–97 °C [29], the achieved denaturation temperature falls well within the range. Therefore, the observed thermal gradient at 95 °C should not affect adversely the amplification efficiency while the total amplification time can be reduced by using a short denaturation step. Fig. 6C demonstrates the thermal gradient at annealing and extension temperatures. The static

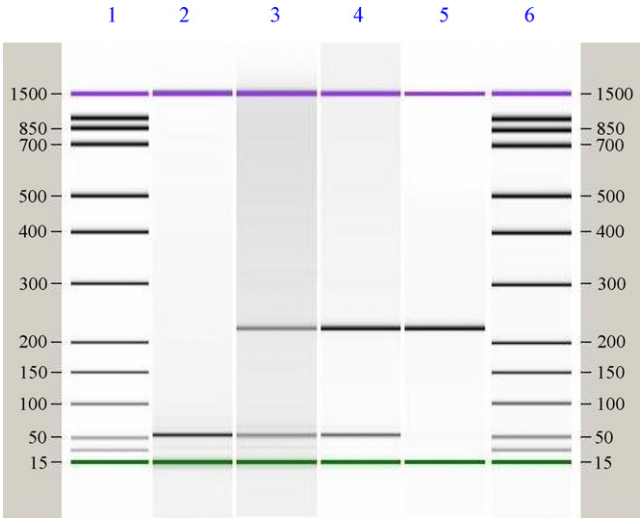

Fig. 7. Amplification of *E. coli* ATCC 35401 *tuf* gene. Lanes 1 and 6: markers; lane 2: negative control; lanes 3–5: amplifications of 10, 100, 1000 genome copies of *E. coli tuf* gene.

temperature difference at these temperatures was as small as 0.2 °C. Thus, high thermal homogeneity, which is critical for the amplification efficiency and specificity, can be attained in the reactor.

3.5. Gain scheduling control

Since the system response was found to be globally nonlinear, a gain schedule with three different sets of PID parameters were used for piecewise linear control so as to attain optimal control at each working temperature (e.g. 60 °C, 72 °C, and 95 °C). In addition, three PD controllers were also included in the gain scheduler specifically for rapid temperature transition [30]. By combining PID and PD control using the gain scheduling scheme, precise control was maintained at each temperature while aggressive temperature transitions were still achieved. The control scheme we developed is an indispensable factor for the optimal control and rapid thermal cycling.

3.6. Amplification of E. coli ATCC 35401 tuf gene

Fig. 7 shows a gel image from the Agilent BioAnalyser 2100 after a 40-cycle amplification. The 210 bp bands corresponding to three template concentrations had demonstrated not only the success of amplification of the target gene, but the well-controlled specificity of amplification. It should also be noted that the temperature profile used in the amplification was not optimized.

4. Conclusions and future work

A disposable PCR card and a Peltier thermal cycler were developed in this work for rapid DNA amplification. Ice valves were used to seal the reaction chamber during thermal cycling. Commercially available Al foils and PP films were laminated with a structured PC card by taking advantage of the adhesives on the foil/film and no extra bonding steps were needed. Numerical modeling was conducted to optimize the design of the PCR reactor and investigate the thermal gradient in the reaction chamber. The PCR reactor was experimentally characterized by using thin foil thermocouples and validated by an amplification of *E. coli* ATCC 35401 *tuf* gene in 27 min. For future work, we will integrate the miniaturized PCR reactor into a centrifuge platform [31–33] with sample preparation and DNA hybridization steps so as to shrink the multiple step bench-top DNA detection assays to a CD (compact disc) μTAS (Micro-Total Analysis System) that is practically affordable for molecular diagnostics.

Acknowledgement

The authors gratefully thank Genome Canada and Génome Québec for the funding of this project.

References

[1] Ice Valve is a patented technology of Aerospace Corp, El Segundo, CA and exclusively licensed by Phasiks Inc. El Segundo, CA.
[2] R.K. Saiki, S. Scharf, F. Faloona, K.B. Mullis, G.T. Horn, H.A. Erlich, N. Arnheim, Science 230 (1985) 1350.
[3] C.T. Wittwer, G.C. Fillmore, D.J. Garling, Anal. Biochem. 186 (1990) 328.
[4] A.J. DeMello, Nature 422 (2003) 28.
[5] J. Cheng, M.A. Shoffner, G.E. Hvichia, L.J. Kricka, P. Wilding, Nucl. Acids Res. 24 (1996) 380.
[6] J.H. Daniel, S. Iqbal, R.B. Millington, D.F. Moore, C.R. Lowe, D.L. Leslie, M.A. Lee, M.J. Pearce, Sens. Actuators A: Phys. 71 (1998) 81.
[7] I. Schneegass, R. Brautigam, J.M. Kohler, Lab Chip 1 (2001) 42–49.
[8] A.T. Woolley, D. Hadley, P. Landre, A.J. deMello, R.A. Mathies, M.A. Northrup, Anal. Chem. 68 (1996) 4081.
[9] D.S. Yoon, Y.S. Lee, Y. Lee, H.J. Cho, S.W. Sung, K.W. Oh, J. Cha, G. Lim, J. Micromech. Microeng. 12 (2002) 813.
[10] M.A. Northrup, B. Benett, D. Hadley, P. Landre, S. Lehew, J. Richards, P. Stratton, Anal. Chem. 70 (1998) 918.
[11] M.A. Burns, C.H. Mastrangelo, T.S. Sammarco, F.P. Man, J.R. Webster, B.N. Johnson, B. Foerster, D. Jones, Y. Fields, A.R. Kaiser, D.T. Burke, Proc. Natl. Acad. Sci. U.S.A. 93 (1996) 5556.
[12] T.B. Taylor, E.S. WinnDeen, E. Picozza, T.M. Woudenberg, M. Albin, Nucl. Acids Res. 25 (1997) 3164.
[13] A. DeMello, Lab Chip 2 (2002) 31N.
[14] J.W. Hong, T. Fujii, M. Seki, T. Yamamoto, I. Endo, Electrophoresis 22 (2001) 328.
[15] Y.S. Shin, K. Cho, S.H. Lim, S. Chung, S.J. Park, C. Chung, D.C. Han, J.K. Chang, J. Micromech. Microeng. 13 (2003) 768.
[16] J.N. Yang, Y.J. Liu, C.B. Rauch, R.L. Stevens, R.H. Liu, R. Lenigk, P. Grodzinski, Lab Chip 2 (2002) 179.
[17] B.C. Giordano, J. Ferrance, S. Swedberg, A.F.R. Huhmer, J.P. Landers, Anal. Biochem. 291 (2001) 124.
[18] H. Wang, J.F. Chen, L. Zhu, H. Shadpour, M.L. Hupert, S.A. Soper, Anal. Chem. 78 (2006) 6223.
[19] J. Wang, Z.Y. Chen, P. Corstjens, M.G. Mauk, H.H. Bau, Lab Chip 6 (2006) 46.
[20] J.F. Chen, M. Wabuyele, H.W. Chen, D. Patterson, M. Hupert, H. Shadpour, D. Nikitopoulos, S.A. Soper, Anal. Chem. 77 (2005) 658.
[21] Z.Y. Chen, J. Wang, S.Z. Qian, H.H. Bau, Lab Chip 5 (2005) 1277.
[22] Y.J. Liu, C.B. Rauch, R.L. Stevens, R. Lenigk, J.N. Yang, D.B. Rhine, P. Grodzinski, Anal. Chem. 74 (2002) 3063.
[23] J. Khandurina, T.E. McKnight, S.C. Jacobson, L.C. Waters, R.S. Foote, J.M. Ramsey, Anal. Chem. 72 (2000) 2995.
[24] http://www.ferrotec.com/products/thermal/modules/
[25] R.B. Bird, W.E. Stewart, E.N. Lightfoot, Transport Phenomena, 2nd ed., John Wiley & Sons, New York, 2002, p. 377.

[26] F.P. Incropera, D.P. Dewitt, Heat and Mass Transfer, 5th ed., John Wiley & Sons, New York, 2002.
[27] B.H. Weigl, J. Gerdes, P. Tarr, P. Yager, L. Dillman, R. Peck, S. Ramachandran, M. Lemba, M. Kokoris, M. Nabavi, F. Battrell, D. Hoekstra, E.J. Klein, D.M. Denno, Microfluidics, BioMEMS, and Medical Microsystems IV, Proceedings of SPIE, San Jose, CA, January 23–25, 2006, pp. 611202–611211.
[28] C.T. Wittwer, G.B. Reed, K.M. Ririe, Rapid cycle DNA amplification, in: K.B. Mullis, F. Ferre, R.A. Gibbs (Eds.), The Polymerase Chain Reaction, Birkhauser, Boston, 1994, pp. 174–181.
[29] C.T. Wittwer, D.J. Garling, Biotechniques 10 (1991) 76–83.
[30] I. Erill, S. Campoy, J. Rus, L. Fonseca, A. Ivorra, Z. Navarro, J.A. Plaza, J. Aguilo, J. Barbe, J. Micromech. Microeng. 14 (2004) 1558–1568.
[31] J. Kim, S.H. Jang, G.Y. Jia, J.V. Zoval, N.A. Da Silva, M.J. Madou, Lab Chip 4 (2004) 516–522.
[32] G.Y. Jia, K.S. Ma, J. Kim, J.V. Zoval, R. Peytavi, M.G. Bergeron, M.J. Madou, Sens. Actuators B: Chem. 114 (2006) 173–181.
[33] R. Peytavi, F.R. Raymond, D. Gagne, F.J. Picard, G. Jia, J. Zoval, M. Madou, K. Boissinot, M. Boissinot, L. Bissonnette, M. Ouellette, M.G. Bergeron, Clin. Chem. 51 (2005) 1836–1844.